Shangkum *et al.*: Nigerian Journal of Materials Science and Engineering. Vol. 11(1):1 - 13 (2021)

# Nanofiltration Performance of a Functionalized UiO-66 Membrane

Shangkum, Yildun Goji*; Solomon, Philip; Rotbe, Gurumji[b]; Lawal, Rabiat Abdullahi; Ranga, Yusuf Garba; Gongden, Joel Japhet; Yoila, Dakup Kitgak; Simon, Kwene Dangkat.

*Department of Chemistry, Faculty of Natural Sciences, University of Jos, P.M.B 2084, Jos. Plateau State, Nigeria.
[a]Plateau State College of Agriculture, Garkawa, P.M.B 001, Mikang, Plateau State, Nigeria.

*Corresponding author: gshangkum@gmail.com; gojis@unijos.edu.ng.

**Abstract**
This research investigates the design principle for metal organic frameworks (MOF) deposited composite membranes for nanofiltration using functionalized/modified UiO-66 (UiO stands for University of Oslo) nanoparticles for the purpose of exploring the importance of functional groups around the nanopores. The nanoparticles were synthesized using water as modulator and characterized by XRD, FTIR, TEM, BET and TGA. The XRD major (sharp) peaks indicated the crystallinity of the nanoparticles whilst the minor peaks at $2\theta = 6°$ originated from reo-nanoregions. The intensity of the reo peak was correlated with the concentration of missing clusters/linkers, cluster defects in the samples and become prominent as small amount of modulator was added. The particle sizes were found to be in the range of 150-60 nm, 160-60 nm for UiO-66-$NH_2$, UiO-66-$CH_3$ frameworks respectively. The dependence of the particle size on the amount of water demonstrated its role to accelerate the formation of crystal nuclei. The BET surface area and pore volume were found to be in the range of 800-1000 $m^2/g$ and 0.37-0.44 $m^3/g$ without clear tendency on the framework type. The pore size distribution was sharply concentrated in the range of 0.7-0.8 nm whilst the weight loss due to ligand decomposition was found to have changed by the water addition irrespective of the ligand functionalization. The functionalized UiO-66 formed polycrystalline, defective nanoparticles and gave high flux compared to non-functionalized type and was found to be superior for leakage tolerance irrespective of the frameworks. However, the tendency to leakage was found to be greater for smaller particle size. Its polycrystalline nature played an important role whilst the modification affects the chemoselectivity and permeation. The pore engineering geared towards changing the chemical environment played significant effects and unlock information for proper understanding of the role of chemical environment in UiO-66-$CH_3$ and UiO-66-$NH_2$ nanocomposite membranes.

**Keyword:** Functionalized UiO-66 nanoparticle, Nanocomposite, Nanopores, Nanofiltration, Chemoselectivity.

## 1. INTRODUCTION

Composite mmembranes designed for nanofiltration utilizes pressure driven processes to remove sub-micron or sub-nanometer scale solutes from a feed stream (e.g. cell debris from a biomolecule solution, hydrated salts from water) based on the solution-diffusion mechanism (Eddaoudi *et al*., 2002; Furukawa *et al*., 2013; Zhang *et al*., 2014; Guo and Peng, 2018). Recent research interests in the area have been directed towards the designing of a new class of membranes, which utilize engineered nanoparticles with well-defined and/or oriented pores/ channels for higher permeability and rejection (Wang *et al*., 2016; Cui *et al*., 2017).

The design of composite membranes based on deposition of chemically stable UiO-66 on porous polymer substrate has recently been discovered as a promising approach which resulted in highly permeable, size-selective, stable, and flexible composite membranes (Furukawa *et al*., 2010; Liu *et al*., 2015; Wu *et al*., 2017; Danchen *et al*., 2017). The remarkable performances of these composite membranes in nanofiltration processes are due to the ability of the deposited nanoparticles to offer a pore network in form of the nanochannels (Cavka *et al*., 2008; Kandiah *et al*., 2010; Cheng *et al*., 2017). These deposited nanoparticles have been found to enhance the hydrophilicity and antifouling characteristics of the polymeric substrate and most importantly offer a predominant permeation network for filtrates with excellent rejection ability for solutes at low operating pressure through the nanochannels (Valenzano *et al*., 2011; Tang and Yan, 2017). For instance, a novel method to form MOF-based composite membrane for nanofiltration where the suspension of a stable frameworks UiO-66 nanoparticles was strategically developed by deposition onto a regenerated cellulose (RC) support membrane via suction filtration (Trinh *et al*., 2017). The nanoparticles were found to fill the pore network and shown to have exhibited an excellent permeability of 7860 ±374 $L/m^2$ h and 100% rejection of a methylene blue (MB) aqueous solution. The performance was attributed to dominant selective nanochannels of deposited UiO-66 in contrast to the non-selective leakage through interparticle voids of the nanoparticles. A semi-continuous selective layer of composite membranes was designed using series of UiO-66

nanoparticles with different average particle sizes (Goji *et.al*., 2018). These were synthesized using water as a modulator that aid in the nucleation and growth of the nanoparticles. It was found that the size and packing of the UiO-66 nanoparticles had great influence on the performance of the composite membranes for the filtration of MB solution. Smaller nanoparticles with a greater external surface area provided a selective layer with superior flux and rejection, while the larger nanoparticles afforded a selective layer having more tolerance for fouling.

Given vast possibilities that other MOF materials could offer in terms of design due to their intrinsic hybrid nature, researches have revealed the use of other nanochannels materials such as carbon nanotubes (Liu *et al.*, 2016; Wan *et al.*, 2017). Nevertheless, in most of these experimentally designed membranes for filtration purposes, the investigations have been geared mainly towards understanding the process of size sieving mechanism, physical aspect of MOFs on filtration performance like surface area, pore size and pore volume.

Thus, the influences of chemical environment around the pore on the permeation and selectivity in filtration need to be systematically investigated. However, this has rarely been examined for MOF based composite membranes (Zornoza *et al.*,2011; Liu *et al.*,2017). Paradoxically, few studies to date have reported the influence of hydrophilicity of functional groups on the pore surface or trace the in-pore chemistries within UiO-66-MOFs and other nanochannels materials on their filtration performance. Though studies of the influence of MOF pore environments on solute molecular dynamics is difficult, it is essentially important for understanding of the intrinsic selectivity properties for improving MOF design practices and grasping the nature of interactions (Aimar *et al.*, 1990; Sharma and Chellam, 2005).

In general, the primary factors that affect performance of membranes are physical, chemical nature of materials, interaction between selective layer and support membrane, concentration polarization and fouling (Bruggen *et al*., 1999; Le-Clech *et al*., 2006; Kandiah *et al*., 2010). However, pore size alone does not fully control the rejection of solute constituents and no studies have been done so far on the importance of functionalized chemical environment around the nanopores. Therefore, this research is aimed at systematic investigation on the design principle for MOF-deposited composite membranes for nanofiltration, achieved through:

i. Tuning of pore environment of nanoparticles via manipulation using functionalized ligands 2-amino/ methyl-terephthalic acids linkers for the synthesis.

ii. Exploring the influence of functionalized UiO-66 nanoparticle on nanofiltration and chemical selectivity.

## 2. EXPERIMENTAL

### 2.1 Materials and methods

Zirconium tetrachloride ($ZrCl_4$, 99%) and 2-amino terephthalic acid (99%) were purchased from Sigma-Aldrich. 2-Methylterephthalic acid (97.2%) was obtained from J &H Chemicals Co. Ltd. N, N-dimethylformamide (DMF) and methanol (MeOH) as solvents were purchased from Wako Chemical Industries Ltd. Methylene blue (MB, 98.5%) was purchased from Kanto Chemical Co Inc. Regenerated cellulose membrane (RC 58, diameter 47 mm and pore size 0.2 μm) was obtained from Whatmann G.E Healthcare, Germany and was used as a support membrane. Deionized (DI) water was used throughout the experiments.

### 2.2 Preparation of UiO-66-X nanoparticles and composite membranes

Solution of $ZrCl_4$ (1.63 mmol) in 30 mL of DMF was added to a solution of 2-aminoterephthalic acid (28 mmol) in 30 mL of DMF under a controlled supply of $N_2$ gas. The chemicals were then mixed in an ultrasonic bath. Thereafter, a specified amount of DI water 0.1-1.2 mL was added and the mixture was heated at 100 °C for 12 h with constant stirring to yield a yellowish dispersion of UiO-66-$NH_2$. The products were isolated by centrifugation and washed with MeOH to completely remove the residual DMF. The solvent was exchanged with 50 mL of fresh MeOH each day for three consecutive days. The purified samples were dried under vacuum at 90 °C for 24 h and the samples were named as UiO1-$NH_2$ –UiO6-$NH_2$ corresponding to the addition of 0.9, 0.7, 0.6, 0.5, 0.3, 0.1 mL. Similarly, UiO-66-$CH_3$ nanoparticles was synthesized by adding a solution of $ZrCl_4$ (1.63 mmol) in 30 mL of DMF to a solution of 2-methylterephthalic acid (1.5 mmol) and mixed in an ultrasonic bath. A specified amount of DI water 0.1-1.2 mL was added to the mixture and then heated at 100 °C under a controlled supply of $N_2$ gas for 12 h with constant stirring to yield a milky dispersion. The products were then isolated by centrifugation, washed with MeOH to completely remove the residual DMF and the solvent was exchanged with 50 mL of fresh MeOH each day for three consecutive days. The purified samples were dried under vacuum at 90 °C for 24 h) and the samples were named as UiO1-$CH_3$ –UiO6-$CH_3$ corresponding to 1.2, 0.9, 0.7, 0.6, 0.5, 0.3 mL of water added respectively (Trinh *et al*., 2017; Goji *et al*., 2018).

Composite membranes of UiO-66-X (X= $NH_2$, $CH_3$) nanoparticles were prepared by suction filtration. A regenerated cellulose (RC) substrate membrane was placed on a filter glass holder and wet with DI water. A specified amount of the nanoparticles was dispersed in 30 mL of DI water by sonication for 1 h, and then deposited on the pre-wetted RC support substrate by suction filtration at a constant differential pressure of 50 mbar. After 30 min of filtration, the differential pressure was increased to 100 mbar and kept for 15 min to partially dry the membrane.

### 2.3 Characterization of UiO-66-X nanoparticles and Composite Membranes

The crystalline structure of UiO-66-X (X=$NH_2$/$CH_3$) nanoparticles was analyzed by X-ray diffraction (XRD, Rigaku Smart Lab) using Cu Kα radiation in the range of 2θ = 5-35° at the step increment of 0.1° per 150 s. The crystallite size (D) of the nanoparticles was estimated using Scherrer's equation:

$$D = \frac{0.94\lambda}{\beta \cos\theta} \quad (1)$$

where λ = 1.54 Å for Cu Kα, b= full-width at half-maximum, and θ = Bragg's angle (Schaate *et al.,* 2011). The dried sample was mixed with potassium bromide powder and pressed into a pellet for the measurement in the transmission mode using Fourier transform infrared spectroscpy (FTIR) on a JASCO FTIR-6100 spectrometer in the range of 400−2400 $cm^{-1}$ at resolution of 4 $cm^{-1}$. The dried sample was dispersed in MeOH and deposited onto a copper grid by drop casting and then dried under air to evaporate the solvent and morphology of UiO-66-X nanoparticle observed on a transmission electron microscope (TEM, Hitachi H6750) at an accelerated voltage of 100 Kv whilst the particle size was obtained based on the TEM image analysis using ImageJ software. About 30 mg of a sample was charged into a sample cell and sealed with brass filler and rubber cap. The sample was outgassed at 180 ºC for 24 h in vacuum and measured using $N_2$ adsorption/desorption at 77 K on BELSORP mini-HS II instrument BEL JAPAN, Inc. The surface area was calculated by fitting the isotherm data in the $P/P_o$ range of 0-1 using Langmuir model that was in-built in a BELMaster7™ software. The sample was loaded on an alumina pan and the TGA measurements were run on a ThermoPlus EVO II (Rigaku) thermal analysis and heated to 800 °C at a temperature ramping rate of (10 °C/min) under a flow of dry air at the rate of 100 mL/min.

The morphology of the prepared composite membranes was observed by a scanning electron microscope (SEM, Hitachi S-4100) operated at an accelerated voltage of 20 kV.

### 2.4 Filtration performance

The composite membrane was placed in a filtration cell of 100 mL and aqueous solution of MB (1.0 μM) was suction filtered at a differential pressure of 100 mbar. A fixed volume of the filtrate was sampled every 1 or 2 min and the concentrations in the feed and permeate solution were determined by UV-Vis spectroscopy (JASCO V670) measurements based on the absorption intensity at 665 nm wavelength. The rejection (R) was calculated using equation.

$$R\,(\%) = \left(\frac{C_0 - C_p}{C_0}\right) \times 100 \quad (2)$$

The flux was determined from the cumulative permeate volume at the specified filtration time as shown in Equation. (3):

$$J = \left(\frac{V}{A \times t}\right) \quad (3)$$

where J represents the flux ($L/m^2$ h), V is the cumulative permeate volume, A is the effective membrane area (calculated as 9.61 $cm^2$), and t is the filtration time (Bruggen *et al*., 1999; Trinh *et al*., 2017; Goji *et al*., 2018). The results were obtained as an average from at least two filtration experiments using independently prepared membranes.

## 3. RESULTS AND DISCUSSION

### 3.1 Preparation and Characterization of UiO-66-X nanoparticles

The peaks at 2θ = 7.4, 8.8, 12.2° corresponded to (111), (200), (222) planes, respectively as shown in Figure 1a**.** These peaks demonstrated good agreement with UiO-66 parent crystal, and confirmed the pure crystal phase formation (Kandiah *et al*., 2010; Huang *et al*., 2012). The minor peaks at 2θ = 6° originated from **reo**-nanoregions as observed by Goodwin and co-workers (Cliffe *et al*., 2014). The intensity of the **reo** peak is correlated with the concentration of missing cluster defects in the samples which originated from missing clusters/linkers and become prominent in the absence of sufficient amount of modulator. For UiO-66-$CH_3$, the peaks at 2θ = 7.4, 8.7, 12.1° corresponded (111), (200), (311) planes respectively. The reo-nanoregions (secondary crystalline phase) was also observed at 2θ = 5.9°, which showed an increasing intensity as the water amount decreases (Figure 1b**)**. However, at highest water amount, the peak intensity of the **reo**-nanoregions significantly reduced and it was observed that the use of water as modulator significantly enhance crystallinity in both UiO-66-$CH_3$ and UiO-66-$NH_2$ because it accelerated the nucleation rate of $Zr_6O_4(OH)_4$ cluster by sol-gel reaction leading to growth of crystals (Huang *et al.*, 2012; Wu *et al*., 2013).

The functional groups present in the prepared samples are as assigned in Figure 2. From the Figure 2a**,** it is possible to distinguish between two characteristic bands of amino group: the medium intensity of $NH_2$ bending vibration observed at 1338 $cm^{-1}$, 1428 whilst strong C-N stretching vibration aromatic amines observed at 1258 $cm^{-1}$. The bands at 1567 $cm^{-1}$ and 1385 $cm^{-1}$ corresponded to symmetric and asymmetric stretching of O-C-O in the carboxylate groups coordinated with zirconium metal centre while band at 1498 $cm^{-1}$ is ascribed to C=C vibration of the aromatic ring (Cliffe *et al*., 2014; Cavka *et al*., 2008; Liu *et al*., 2016; Taddei *et al*., 2017). The characteristic band at 765 $cm^{-1}$ is ascribed to a mixture of OH and C-H vibrational bendings (Liu *et al*., 2016) whilst those at 664, 655, 473 $cm^{-1}$ are assigned to Zr (O-C) streching and $m_3$-OH streching, which indicates successful synthesis of UiO-66-$NH_2$. The FTIR spectrum of UiO-66-$CH_3$ (Figiure 2b) was compared with parent UiO-66 sample and showed strong out-of-phase carboxylic -CO- peak at 1496 $cm^{-1}$, and O-C-O stretchings at 1581 $cm^{-1}$ indicating co-

ordination of terephthalic acid ligand with zirconium metal. The strong doublet peaks at 1378 $cm^{-1}$ and 1407 $cm^{-1}$ represent the C-C vibration of $CH_3$ of aromatic ring. The peak at 762 $cm^{-1}$ was ascribed to OH and C-H vibrational bendings (Liu *et al*, 2016) whilst bands at 664 $cm^{-1}$, 567 $cm^{-1}$, 467 $cm^{-1}$ are assigned to Zr (O-C) streching and $m_3$-OH streching and indicated successful synthesis of UiO-66-$CH_3$ (Liu *et al,*, 2006; Cavka *et al*., 2008; Nan *et al*., 2012; Cheng *et a.l*, 2017).

The particle sizes were acquired from TEM images using ImageJ software as listed in Table 1. SEM average sizes of the particles of UiO-66-$NH_2$ were found to distributed in the range between 150-60 nm (Table 1). Though not perfect, the particle sizes were found to increase with the decrease in the quantity of water added as shown by the XRD crystallite size measured from the XRD data. The dependence of the particle size on the amount of water demonstrated the role of water to accelerate the formation

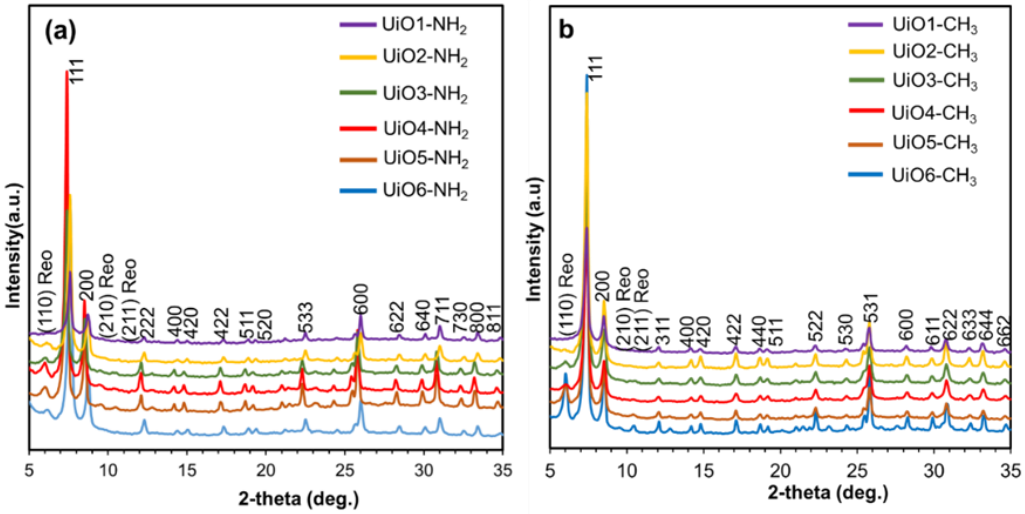


**Figure 1:** XRD patterns of modified UiO-66 samples: a) UiO-66-$NH_2$ b) UiO-66-$CH_3$ nanoparticles

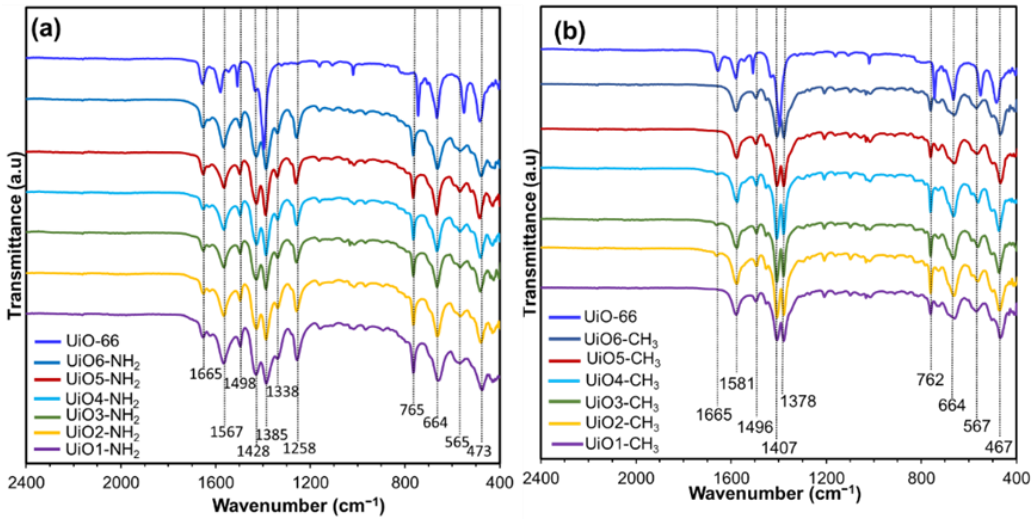


**Figure 2:** IR spectra of modified UiO-66 samples: UiO-66-$NH_2$ and UiO-66-$CH_3$ nanoparticles

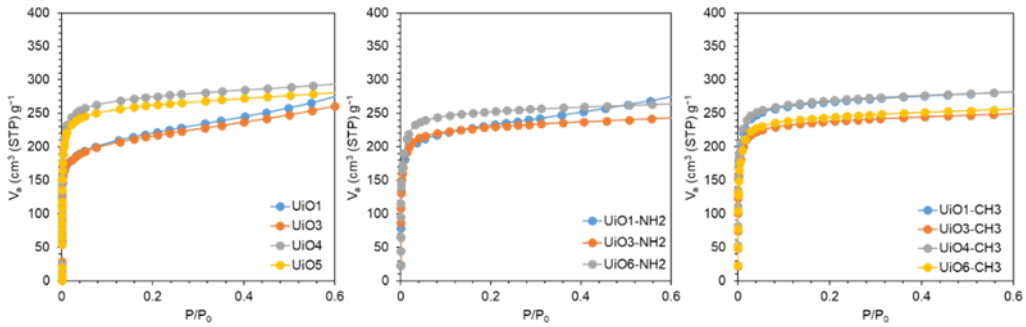


**Figure 4:** $N_2$ adsorption/desorption isotherms of some selected nanoparticles

**Table 1:** Size Analysis of UiO-66-X nanoparticles

| Sample | Water amount[a] (mL) | Crystallite size from XRD[b] (nm) | Particle size from TEM[c] (nm) | Sample | Water amount[a] (mL) | Crystallite size from XRD[b] (nm) | Particle size from TEM[c] (nm) |
|---|---|---|---|---|---|---|---|
| UiO1-$NH_2$ | 0.90 | 40 | 61±14 | UiO1-$CH_3$ | 1.2 | 43 | 89±11 |
| UiO2-$NH_2$ | 0.70 | 41 | 78±08 | UiO2-$CH_3$ | 0.9 | 34 | 107±08 |
| UiO3-$NH_2$ | 0.60 | 51 | 98±11 | UiO3-$CH_3$ | 0.7 | 35 | 109±12 |
| UiO4-$NH_2$ | 0.50 | 59 | 113±09 | UiO4-$CH_3$ | 0.6 | 40 | 115±14 |
| UiO5-$NH_2$ | 0.30 | 88 | 124±16 | UiO5-$CH_3$ | 0.5 | 41 | 138±21 |
| UiO6-$NH_2$ | 0.10 | 51 | 142±07 | UiO6-$CH_3$ | 0.3 | 47 | 151±19 |

[a]Water amount added; [b]Determined using Scherrer's equation based on the (002) plane. [c]Median particle size acquired from TEM images using ImageJ software.

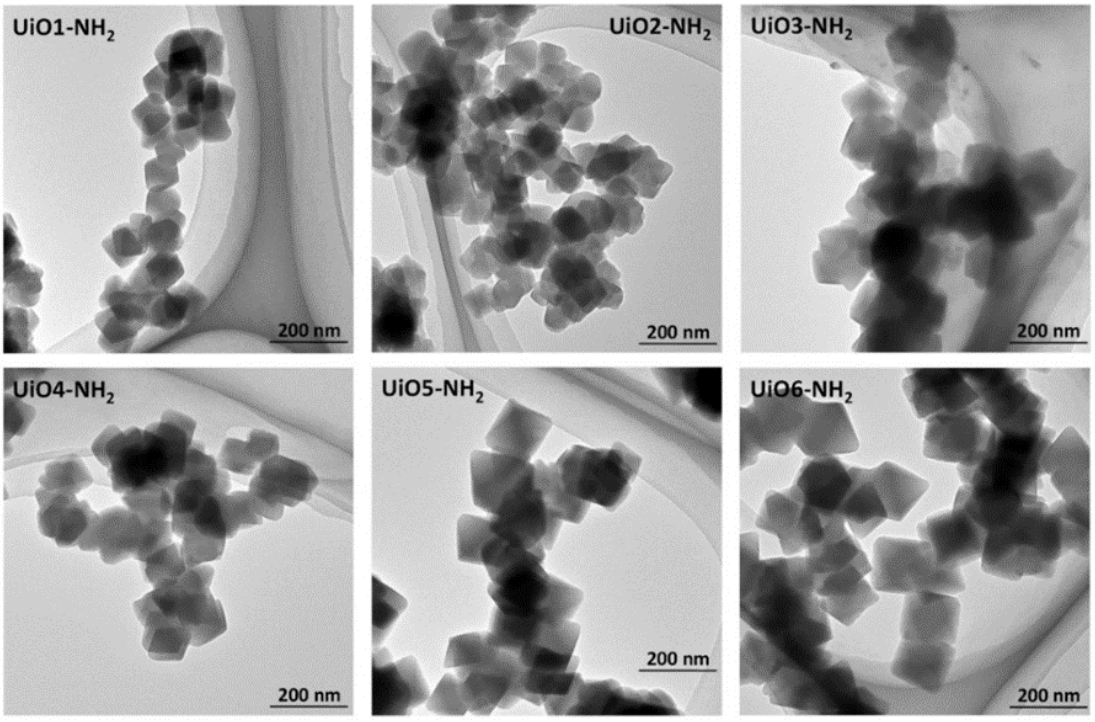


**Figure 3a:** TEM images of UiO-66-$NH_2$ nanoparticles

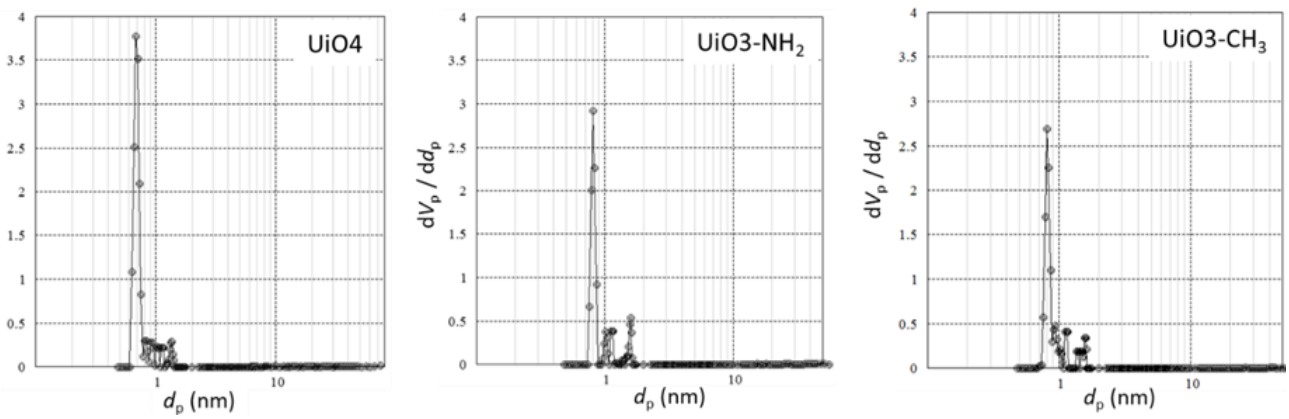


**Figure 5:** Pore size distribution for selected samples nanoparticles

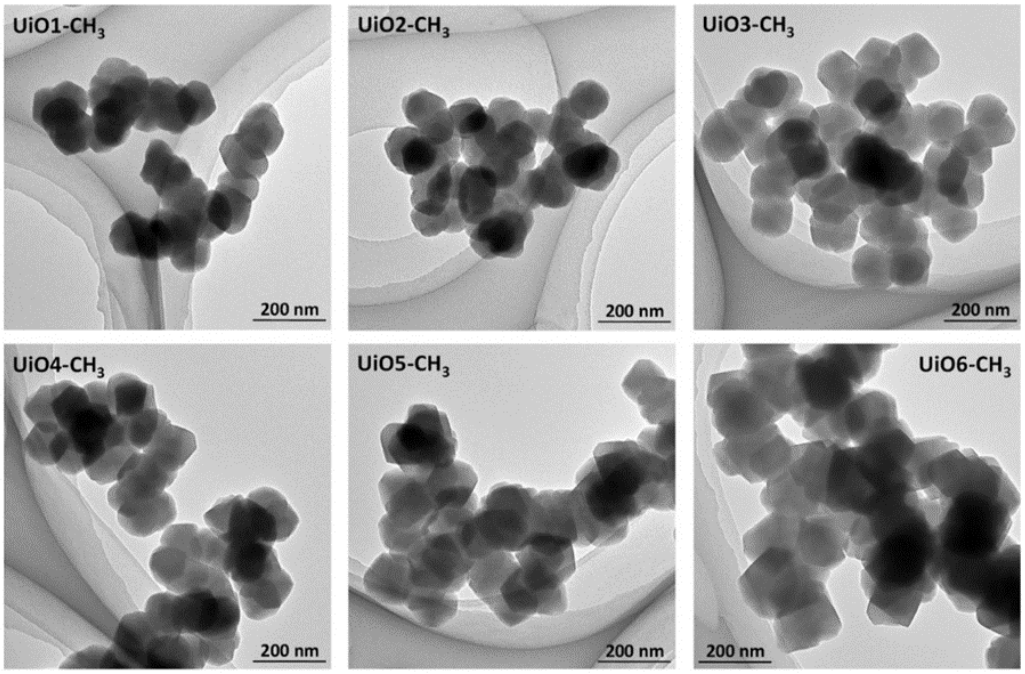


**Figure 3b:** TEM images UiO-66-$CH_3$ nanoparticles

| Sample | BET surface area ($m^2$/g) | Pore volume at P/P0 = 0.4 ($cm^3$/g) |
|---|---|---|
| UiO1 | 803 | 0.380 |
| UiO3 | 799 | 0.367 |
| UiO4 | 1060 | 0.442 |
| UiO5 | 1010 | 0.422 |
| UiO1-NH2 | 861 | 0.390 |
| UiO3-NH2 | 867 | 0.367 |
| UiO6-NH2 | 958 | 0.402 |
| UiO1-CH3 | 1010 | 0.427 |
| UiO3-CH3 | 915 | 0.379 |
| UiO4-CH3 | 1035 | 0.428 |
| UiO6-CH3 | 925 | 0.389 |

**Table 2:** Surface area and pore volume of selected UiO-66, UiO-66-$NH_2$ and UiO-66-$CH_3$ nanoparticles

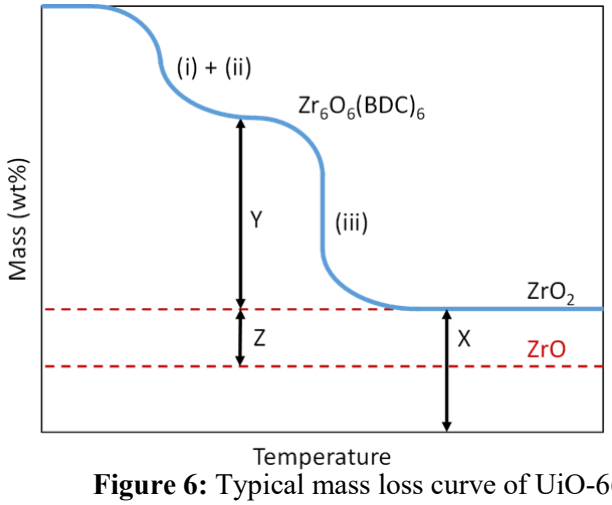


**Figure 6:** Typical mass loss curve of UiO-66

of crystal nuclei (Wu *et al*., 2013; Cliffe *et al*., 2014; Cliffe *et al*., 2015). Depending on the amount of water added, the TEM average size of the UiO-66-$CH_3$ particles was found to vary in the range of 160-60 nm as shown in Table 1. It has been previously reported that the crystallization of UiO-66 became significantly faster in the presence of water because of the ease of the $Zr_6$-cluster formation (Ragon *et al.,*2014). In this study, it was evident by the formation of a more turbid solution when a large amount of water was added during the synthesis.

The morphology of UiO-66-X nanoparticles (X= $NH_2$, $CH_3$) were observed by TEM (Figure 3a, 3b). The crystal morphology in this work was found to be similar to those reported in the literature (Valenzano *et al*., 2011; Morris *et al*., 2017). From Figure 3a, TEM images showed a symmetrical triangular base pyramid crystals morphologies/shapes whilst the particle size of UiO-66-$CH_3$ was found to be dependent on the amount of water added leading to an octahedral (quasi-spherical morphology) of the particles (Diring *et al*., 2010; Oien *et al*., 2014; Morris *et al*., 2017) as shown in Figure 3b.

$N_2$ adsorption/desorption isotherms for the three kind of MOFs frameworks are presented in Figure 4. The adsorption showed a steep increment at a very low relative pressure (below $P/P_o$=0.05) irrespective of frameworks types and water amount. This corresponded to the filling of intraparticle channels where $N_2$ adsorption occurred only through the multilayer adsorption on external surfaces of the nanoparticles. Therefore, the increment became significantly marginal against the pressure. The slight increased in $N_2$ uptake could be attributed to presence of defects in the MOF (Peterson *et al.*, 2017). The BET surface area and the pore volume were respectively estimated in the range of 800-1000 $m_2/g$ and 0.37-0.44 $m_3/g$ without clear tendency on the framework type and the water amount **(**Table 2**).** This fact suggested that the $N_2$ adsorption/desorption behaviors of UiO-66 nanoparticles were mostly originated from those for the perfect crystal.

The pore size distribution of selected samples of different frameworks were calculated using grand canonical Monte Carlo method software as shown in Figure 5. Consistent to $N_2$ adsorption/desorption isotherms; the pore size distribution was not dependent on the amount of water added. Additionally, irrespective of the frameworks or ligand functionalization, the pore size distribution was sharply concentrated in the range of 0.7-0.8 nm, in good agreement with the theoretical pore size.

Thermogravimetric analysis (TGA) was used for estimating the amount of structural defects in MOFs types that is caused by missing clusters/linkers. A typical representation of TGA thermogram for UiO-66 family represented by $Zr_6O_4(OH)_4BDC_6$, (where BDC is 1,4-benzenedicarboxylate linker) is as shown in Figure 6. The heating of UiO-66 under $O_2$ causes three-step mass losses, which are i) solvent evaporation, ii) dehydroxylation, and iii) ligand decomposition. The dehydroxylation is typically completed upto 200-300 °C, and the chemical composition of UiO-66 is changed into $Zr_6O_6BDC_6$. The ligand decomposition usually occur with oxidation of ZrO ($Zr_6O_6$) into $ZrO_2$ as the final product. In both missing linkers and missing clusters, there is reduction of the coordination number of a $Zr_6O_4$ $(OH)_4$ cluster against the BDC (Gutov *et al*., 2015; Shearer *et al*., 2016). From the profile (Figure 6), the mass of the remaining $ZrO_2$ was set to X=1, and the mass gain by the oxidation calculated as:

$$Z = 15.999/123.218 \quad (4)$$

The mass loss by the ligand decomposition is then derived from

$$Y \text{ (observed mass loss)} + 0.130 \quad (5)$$

The average coordination number ($CN_{avg}$) is expressed by

$$CN_{avg} = 12(Y+0.130) \text{ x (MW of } ZrO_2)/(\text{MW of BDC}) \quad (6)$$

For defect-free UiO-66, the mass before the ligand decomposition (X+Y) is theoretically calculated as

$$1 + 12/12 \text{ x (MW of BDC)/ (MW of } ZrO_2) - 0.130 \quad (7)$$

where MW is the molecular weight. This leads to 2.20, 2.45, and 2.53 for normal UiO-66, UiO-66-$NH_2$, and UiO -66-$NH_3$, respectively. One missing linker per cluster (i.e. CN=11) reduces the value of (X+Y) to 2.09, 2.31, and 2.39, respectively. This leads to 2.20, 2.45, and 2.53 for normal UiO-66, UiO-66-$NH_2$, and UiO-66-$CH_3$, respectively.

Figure 7 summarizes the TGA results for the three kinds of UiO-66 nanoparticles, where the mass change relative to the residual $ZrO_2$ was normalized to the remaining contents. The ligand decomposition stability of the framework was in the order of UiO-66-$NH_2$<<UiO-66-$CH_3$<UiO-66. From the decomposition temperatures among the frameworks, the parent UiO-66 frameworks decomposition starts around 350-550 °C while that of UiO-66-$CH_3$, UiO-66-$NH_2$ occurred at 300°C, 400°C, respectively. The lowest stability of UiO-66-$NH_2$ means that it is more defective and was attributed to presence of electron withdrawing group on the benzene ring (Cavka *et al*., 2008; Kandiah *et al*, 2010; Oien *et al.*, 2014). This decrease in decomposition framework is as illustrated in black line (Figure 7) representing theoretical organic decomposition amount for perfect crystals. The weight loss due to ligand decomposition was found to have changed by the addition of water amount whilst the ligand decomposition temperature was independent of the added water. At insufficient water amount, the weight loss tended to be reduced leading to missing linkers and/or clusters. The insufficient water amount might have slowed down cluster formation and thereby bridging incomplete clusters by a ligand to form these defective structures. However, at sufficient addition of water amount, the weight before the

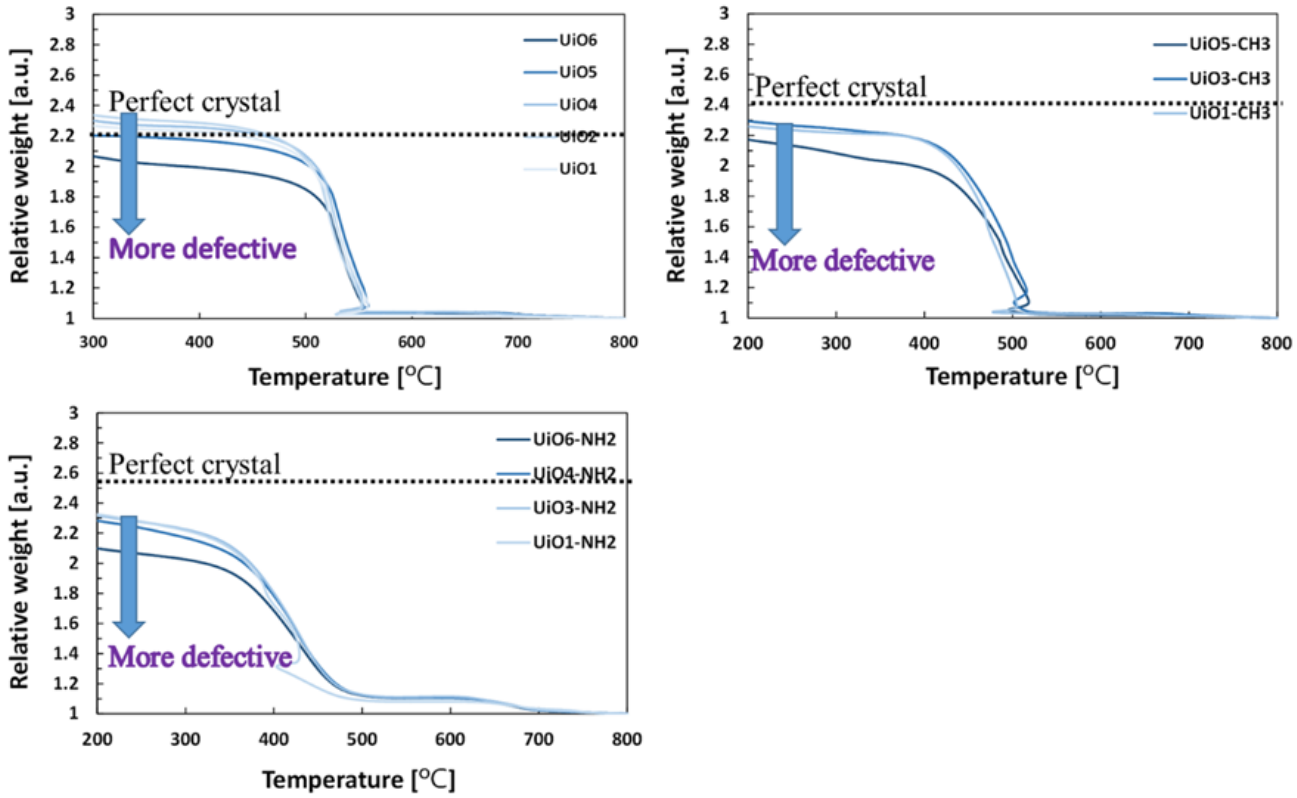


**Figure 7:** Organic content with respect to residual $ZrO_2$ of some selected nanoparticles

ligand decomposition became closer to that of the perfect crystal for un-functionalized UiO-66. For instance, UiO-66-$CH_3$ weight before the ligand decomposition was around 2.3, which corresponded to the coordination number of 10, 11. Similarly, the coordination number was estimated around 11 as in the case of UiO-66-$NH_2$. In this way, the presence of side functional groups enhances the defect formation probably because of increased bulkiness (Liu *et al.*, 2016).

SEM micrograph of composite membranes prepared using UiO1-$NH_2$–UiO6-$NH_2$ shown in Figure 8. They show strange and interesting crystals morphologies for some of UiO-66-$NH_2$ that existed as individual nanoparticles with distinct edges existed and exhibited homogeneous crystalline morphologies that are connected with neighbouring particles. The interconnections among the crystals were found to vary according to water amount used. This revealed small increase in size of interparticle voids as the nanoparticles were homogeneously packed on the substrate membranes. Therefore, packing of smaller particles created no voids on substrate surface as compared to larger particles thereby leading to an efficient nanofiltration performance.

In order to confirm the effects of the functional group modification of the prepared MOF nanoparticles, the XRD crystallite was compared with TEM particle sizes at different water content for the MOF samples to confirm the effects of functional group modification on the crystallinity **(**Figure 9**)**. The particle and crystallite size from TEM and XRD nanoparticles respectively and that of pure UiO-66 nanoparticles (without any modification) were found to be the same and thus, the nanoparticles are believed to be monocrystalline. However, in the case of chemically modified systems, the nanoparticles seem to show polycrystalline behavior which indicated ligand effects where the nucleation rate becomes slower due to the bulkiness of modified ligands as compared to unmodified ligands.

### 3.2 Filtration performance

Filtration performance of ccomposite membranes based on the rejection of MB of some selected UiO-66-$NH_2$ is as presented in Figure 10. The selectivity of UiO-66 composite membranes originated from the molecular sieving ability of the intraparticle channels of UiO-66 (Trinh *et al*., 2017; Goji *et al*., 2018). From the Figure 10, a linear permeation curve along with the perfect MB rejection for the first 5 minutes of filtration was observed. Additionally, the permeability changed with respect to particle resulting into higher permeability with respect to the particle size in systematically increasing pattern.

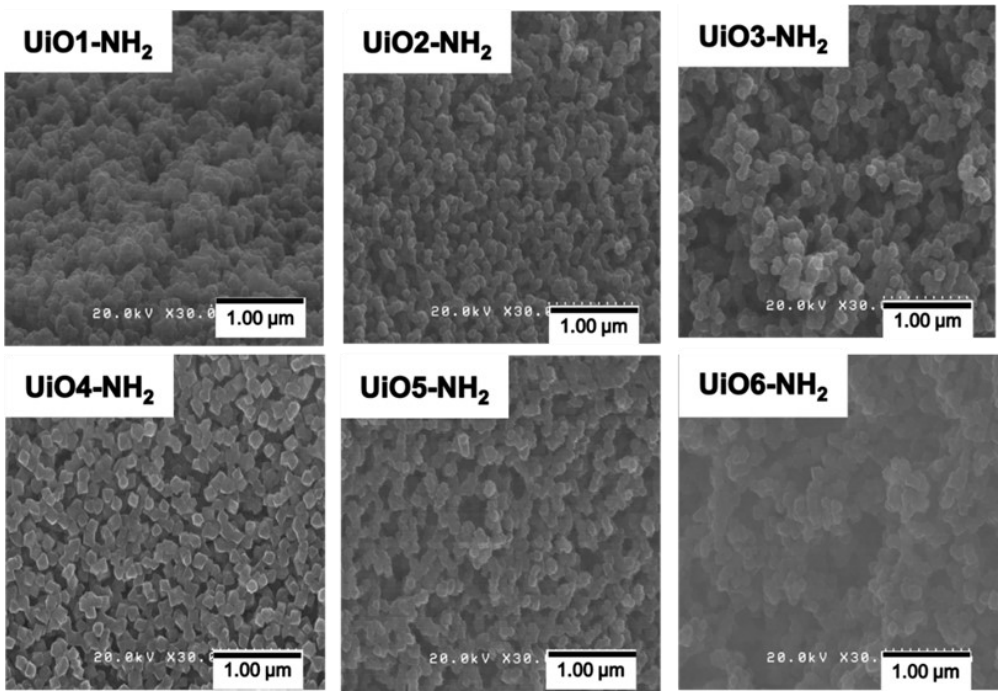


**Figure 8:** Top-view SEM images of the composite membranes: UiO1-$NH_2$ –UiO6-$NH_2$ nanoparticles

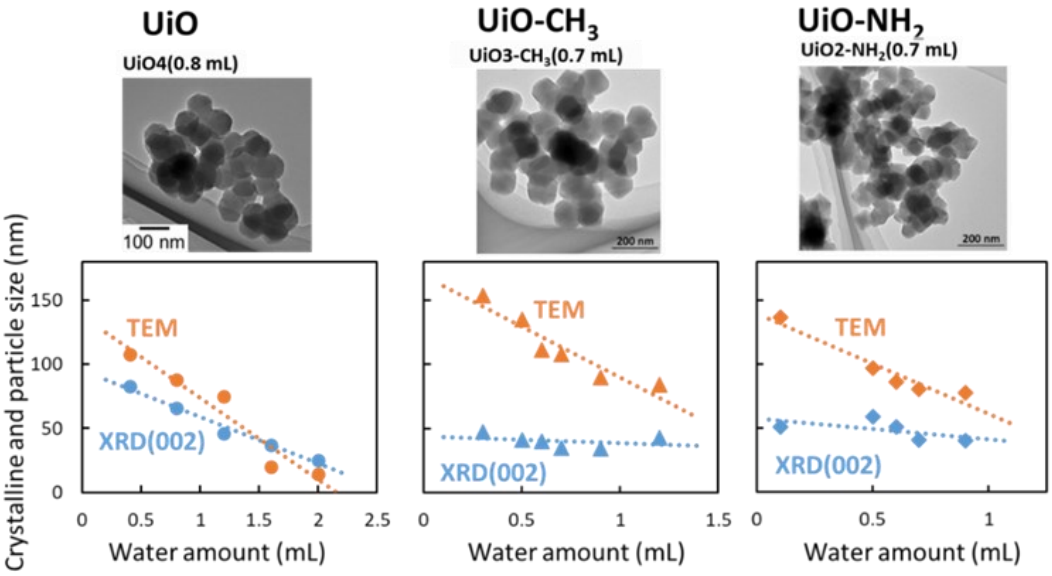


**Figure 9:** Effect of water amount on crystallite (calculated from XRD and particles size from TEM image analysis) of the synthesized nanoparticles

However, for the non-functionalized MOF, the filtration tendency was found to be similar in all cases regardless of the chemical environment around MOF nanoparticles (Goji *et al.*, 2018).

Particle size affect the interactions between selective layer, morphology, surface roughness, and separation performance and therefore should be taken into account when designing a specific composite membrane (Japip *et al.*, 2016). Therefore, the effect of particles size on the flux of non-functionalized and functionalized MOFs, the dependence of the flux on the particle size estimated from TEM images was investigated and plotted as shown in Figure 11a. The flux dependence significantly differed because the functionalized UiO gave larger flux at a given size possibly due to defective structures, which created large aperture of nanochannels. However, the flux for all series of nanoparticles was found to decrease with increase in particle size. Therefore, the trend was similar to that for non-functionalized UiO-66 nanoparticles. Additionally, it is expected that nanoparticle size can enhance

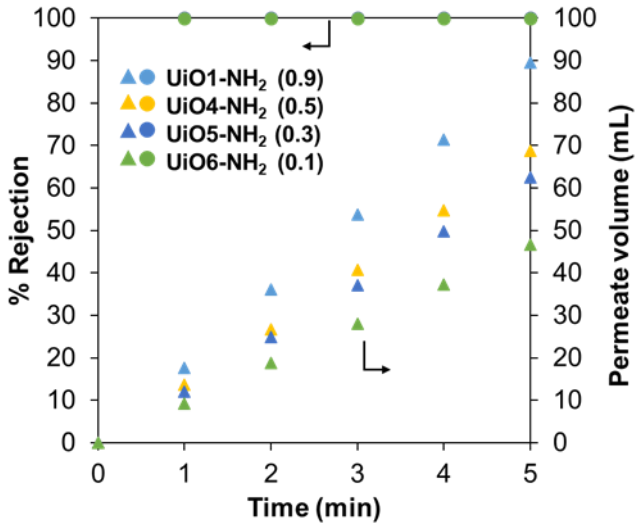


**Figure 10:** Filtration performance of some selected UiO-66-$NH_2$ composite membranes: MB rejection and permeate volume

the filtration greatly. However, the particle size was found not to have represented the flux well. Therefore, crystallite size (from XRD analysis) was plotted against flux (Figure 11b). The trend was found to be better than for TEM particle sizes and affected the flux. This demonstrated that MOF nanoparticles smaller and defective crystals (possess larger pore aperture in the crystallites) were found to be superior in terms of flux due to larger surface area. Thus, modification introduces a larger fraction of defects resulting in an overall higher flux at the crystallite size. Hence, single crystal can be considered as a kind of building unit in the nanoparticles deposition membranes for water filtration.

The filtration performance of these newly synthesized MOF nanoparticles-based membranes was evaluated as shown in Figure 12. The linear permeation curve along with perfect MB rejection for the first 5 minutes of filtration was observed. This remarkable improvement in terms of leakage/fouling was observed due to functionalization of UiO-66 thereby suppressing leakage/fouling. Furthermore, it can also be observed that permeability of the membranes changes with respect to particle size where smaller particles gave higher permeability. Nevertheless, comparing this with the earlier results for non-functionalized MOF membranes, the trend was similar regardless of chemical nature of the resultant MOF as reported for UiO-66 nanoparticles with smallest diameter (Trinh *et al.*, 2017; Goji *et al.*, 2018).

The tolerance ability for leakage of the functionalized particles was determined by keeping the cumulative volume over 99% rejection and the tolerance for MB leakage was estimated (Figure 13). The results indicated that the modified UiO-66 was superior for leakage tolerance and irrespective of the UiO type, the tolerance to leakage was greater for smaller crystallites size. Additionally, the variation in the particle morphology due to ligand modification might have added to this higher tolerance value as a result of dense packing of the selective layer compared to the non-modified MOF based membranes. Therefore, the chemical environment and pore engineering have significant effects on the filtration process.

The transport of water and other solvents through nanochannels materials like MOFs is a complex process and is affected by factors like temperatures, pressures, flow rate and electric fields because of structures, diameter of nanochannels as well as diffusion properties. MOFs with proper pore apertures can be used to elevate the selectivity and permeability of composite membranes (Trinh *et al.*, 1995; Japip *et al.*, 2016). These MOFs composite memranes in an aqueous environment often shows attractive or repulsive response to water and other solvents. For instance, a hydrophilic membrane exhibits an affinity for water due to its high surface tension value and ability to

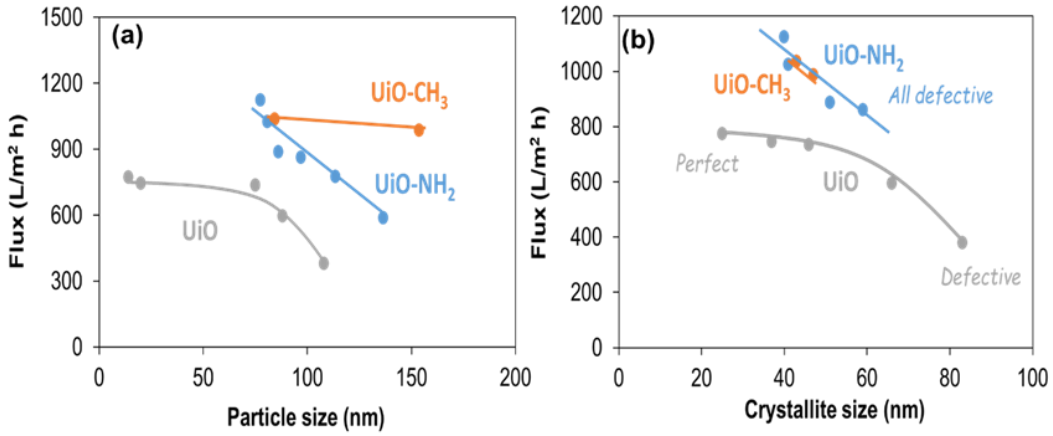


**Figure 11:** Filtration performances a) Effects of different particle sizes on flux b) Effect of crystallite size versus flux

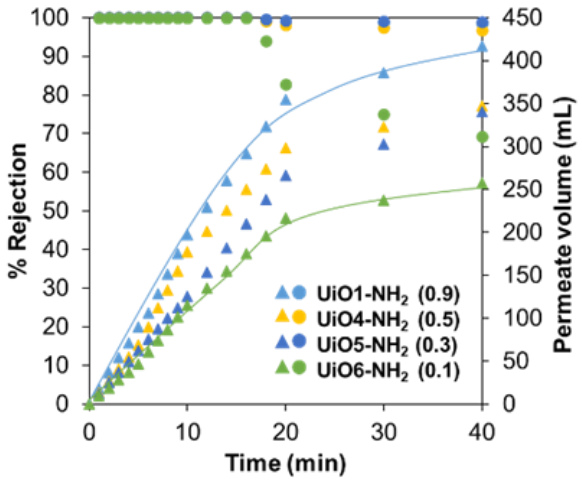


**Figures 12:** Filtration performance of some selected UiO-66-$NH_2$ composite membranes: Leakage and fouling

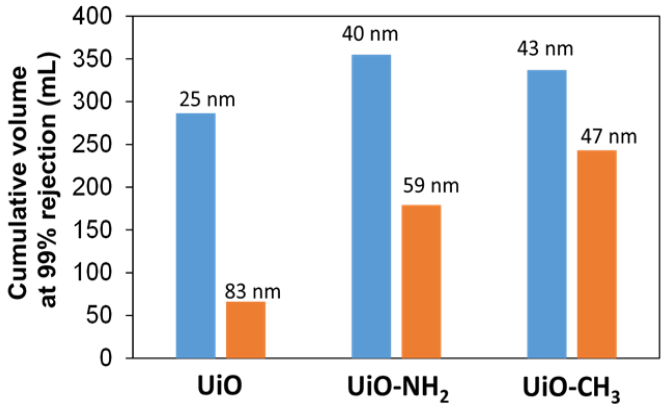


**Figure 13:** Cumulative rejection of composite membrane: Ligand effect on leakage tolerance

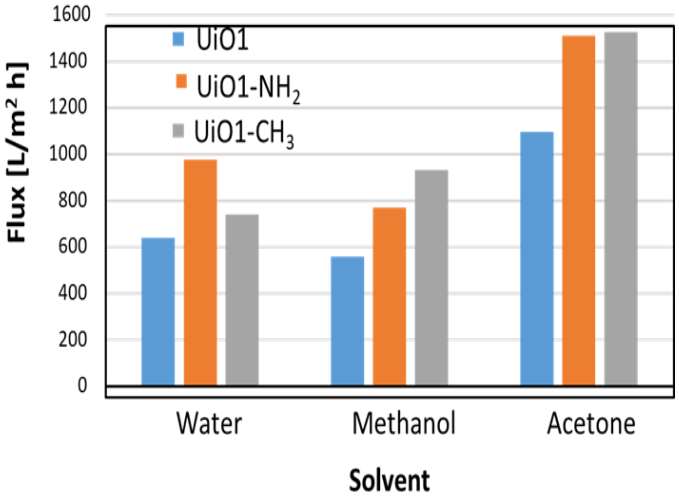


**Figure 14:** Filtration performance: Permeability test of three different composite membranes for solvents.

form "hydrogen-bonds" with water molecules (Mallik *et al.*, 2006; Shen *et al.*, 2016). Additionally, though permeability of solvents such as methanol, ethanol, water, and acetone through composite membranes often depend on the swelling tendency as dominant factors added to solvent physical properties. However, the superiority of composite membranes in terms of permeability and selectivity is attributed to the chemical environment around the nanopores. Therefore, role of chemical environments of unfunctionalized and functionalized nanoparticles was verified by permeation test for methanol, water and acetone with different viscosities *as* 0.56, 0.89, and 0.316 centipoise for methanol, water, and acetone respectively. The solvents permeability through unfunctionalized and functionalized UiO (small particles sizes) is as shown in Figure 14. Though the particle size of UiO1-$NH_2$ and UiO1-$CH_3$ was much bigger than UiO1, flux was found to be comparable or greater. For instance, the flux of acetone was found to be higher because its viscosity is lowest. However, the viscosity of methanol, which is lower, yet its flux comparable to that of water was attributed to hydrogen bonding which enhances water flux in spite its high viscosity and as such channel environment was found to be more sensitive to water than other solvents. The result indicated $NH_2$ accelerates water permeation whilst $CH_3$ decelerate it, thus, hydrogen bonding is important for water intrusion. The order for solvent permanence: acetone > methanol> water; acetone> water > methanol; acetone> water > methanol for UiO1-$CH_3$, UiO1-$NH_2$ and UiO1 composite membrane respectively. Therefore, nanopores environment significantly contributed to the permeate flux differential behaviour. The hydrophilicity/hydrophobicity of UiO-66-$NH_2$/UiO-66-$CH_3$ nanoparticles therefore showed different chemical environment due to functional groups and accounted for high/low water flux due to environment around the nanopores (Su *et al*, 2011; Su *et al*, 2012; He *et al.*, 2017; Liang *et al.*, 2018).

## 4. CONCLUSIONS

UiO-66 nanoparticles with different functional groups were synthesized using water as modulator and the major XRD pattern shows the crystallinity of the nanoparticles whilst the minor peaks at $2\theta = 6°$ which originated from reo-nanoregions. The intensity of the peak was correlated with the concentration of missing cluster defects in the samples. The particle sizes were found to be in the range of 150-60 nm, 160-60 nm for UiO-66-$NH_2$, UiO-66-$CH_3$ respectively and increases with decrease in the amount of water added. The dependence of the particle size on the amount of water demonstrated its role to accelerate the formation of crystal nuclei. The BET surface area and pore volume were found to be in the range of 800-1000 $m^2/g$ and 0.37-0.44 $m^3/g$ without clear tendency on the framework type. The BET surface area and pore volume were found to be in the range of 800-1000 $m^2/g$ and 0.37-0.44 $m^3/g$ without clear tendency on the framework type.

The ligand modification led to the formation of polycrystalline, defective particles and the polycrystalline nature was found to have played an important role as well as modification which affected the chemoselectivity. Thus, the deposition of these nanoparticles not only created an enlarged effective membrane area to minimize the voids pathway that circumvented leakage of solvent, but also accounted for the high flux of water as well as the rejection due to the chemical environment around the nanopore. Pore engineering is therefore a promising approach to improve the membrane performance and to endow it with chemoselectivity properties. Thus, these investigations unlock information for proper understanding, evaluation of the role of chemical environment in UiO-66-$CH_3$ and UiO-66-$NH_2$ nanocomposite membranes.

## 5. ACKNOWLEDGMENTS

Goji Y. Shangkum appreciates the financial support from University of Jos, Nigeria through Need Assessment fund for PhD programme at Japan Advanced Institute of Science and Technology.

## REFERENCES

Aimar, P.; Meireles, M.; Sanchez, V. A (1990). Contribution to the Translation of Retention Curves into Pore Size Distributions for Sieving Membranes. *J. Membr. Sci.*, 54, 321-338.

Bruggen, B.; Schaep, J.; Wilms, D.; Vandecasteele, C. (1999). Influence of Molecular size, Polarity and Charge on the Retention of Organic Molecules by Nanofiltration. *J. Membr. Sci.*, 156, 29-41.

Cavka, J. H., Jakobsen, S. Olsbye, Guillou, N. Lamberti, C. Bordiga, S. Lillerud, K. P.A. (2008). New Zirconium Inorganic Building Brick Forming Metal Organic Frameworks with Exceptional Stability. *J. Am. Chem. Soc.,* 130, 13850-13851.

Cheng, X.; Xu, J.; Yanqui, Z.; Cher, H. L.; Zongli, X.; Derrick, N.; Stefan, J. D.; Metthew, R. H.; Lu, S. (2017). Building Additional Passageways in Polyamide Membranes with Hydrostable Metal-Organic Frameworks to Recycle and Remove Organic Solutes from Various Solvents. *ACS Appl. Mater. Interfaces*, 44, 38877-38886.

Cliffe, M. J.; Hill, J. A.; Murray, C. A.; Coudert, F. X.; Goodwin, A. L. (2015). Defect-Dependent Colossal Negative Thermal Expansion in UiO-66 (Hf) Metal-Organic Framework. *Phys. Chem. Chem. Phys.*, 17, 11586−11592.

Cliffe, M J; Wan, W, Zou, X. Chater, P. A.; Kleppe, A. K.; Tucker, M. G.;Wilhelm, H; Funnell, N. P.; Coudert, F.-X.. Goodwin, A.. L. (2014). Correlated Defect Nanoregions in a Metal-Organic Frameworks. N*at. Commun,* 5, 4176–4178.

Cui, Y. Liu, X. Y; Chung, T. S. (2017). Ultrathin Polyamide Membranes Fabricated from Freestanding Interfacial Polymerization Synthesis, Modifications, and Post-Treatment. *Ind. Eng. Chem. Res. 56*, 513-623.

Danchen, M.; Han, G.; Bo Peh.; Chen, S. B. (2017). Water-Stable Metal–Organic Framework UiO-66 for Performance Enhancement of Forward Osmosis Membrane. *Ind. Eng. Chem. Res.*, 56, 12773-12782.

Deen, W. M. (1987). Hindered Transport of Large Molecules in Liquid Filled Pores. *AIChE J.*, 33, 1409–1424.

Diring, S.; Furukawa, S.; Takashima, Y.; Tsuruoka, T.; Kitagawa, S. (2010). Controlled Multiscale Synthesis of Porous Coordination Polymer in Nano/Micro Regimes. *Chem. Mater.*, 22, 4531−4538.

Eddaoudi, M.; Kim, J.; Rosi, N.; Vodak, D.; Wachter, J.; O'Keeffe, M.; Yaghi, O.M. (2002). Systematic Design of Pore size and Functionality in Isoreticular MOFs and their Application in Methane Storage. *Science,* 295, 468—*472*

Furukawa, H.; Cordova, K. E.; O'Keeffe, M.; Yaghi, O. M. (2013). The Chemistry and Applications of Metal-Organic Frameworks. *Science*, 341, 974.

Furukawa, H.; Ko,N.; Go, Y. Aratani, N.; Choi, S. B.; Choi, E.; Yazaydin, A.O; Snurr, R. Q; O'Keeffe, M.; Kim, J.; Yaghi,O. M. (2010). Ultrahigh Porosity in Metal-Organic Frameworks. *Science*, 424–*428.*

Goji. S. Y.; Trinh X. Dai.; Patchanee, C.; Taniike, T. (2018). Design of Semi-Continuous Selective Layer Based on UiO-66 Nanoparticles for Nanofiltration. *Membr.* 8 129.

Guo, Y.; Peng, X. (2018). Mass Transport through Metal-Organic Framework Membranes. *Reviews. Science China Materials*, 1–*18.*

Gutov, O. V.; Hevia, M. G.; Escudero-Adan, E. C.; Shafir, A. (2015). Metal-Organic Framework (MOF) Defects under Control: Insights into the Missing Linker Sites and Their Implication in the Reactivity of Zirconium-Based Frameworks. *Inorg. Chem.*, 54, 8396−8400.

He, Y.; Tang, Y. P.; Ma, D.; Chun, T. S. (2017). UiO-66 Incorporated Thin-Film Nanocomposite Membranes for Efficient Selenium and Arsenic Removal. *J. Membr. Science*, 541 262–270.

Huang, Y.; Qin, W.; Li, Z.; Li, Y. (2012). Enhanced Stability and $CO_2$ Affinity of a UiO-66-type Metal–Organic Framework Decorated with Dimethyl Groups. *Dalton Trans.*, 41, 9283.

Japip, S.; Xiao, Y.; Chung, T.S. (2016). Particle Size Effects on Gas Transport Properties of 6FDA-Durene/ZIF-71 Mixed Matrix Membranes. *Ind. Eng. Chem. Res.*, 55, 9507–9517.

Kandiah, M.; Nilsen, M.H.; Usseglio, S.; Jakobsen, S.; Olsbye, U.; Tilset, M.; Larabi, C.; Quadrelli, E.A.; Bonino, F.; Lillerud, K. P. (2010). Synthesis and Stability of Tagged UiO-66 ZrMOFs. *Chem. Mater.*, 22, 6632-6640.

Kandiah, N., Usseglio, Svelle S.; Olsbye, S.; Lillerud, K.. P. (2010). Tilset, M. Post-Synthetic Modification of the Metal-Organic Framework Compound UiO-*66. J. Mater. Chem.* 20, 9848-9*8.*

Lee, S.; Lueptow, R. M. (2001). Membrane Rejection of Nitrogen Compounds. *Environ. Sci. Technol.*, 35, 3008–3018.

Liang, W.; Li,L.; Hou, J.; Shepherd, N. D.; Bennett, T. D.; D'Alessandro, D. M.; Chen, V. (2018). Linking Defects, Hierarchical Porosity Generation and Desalination Performance in Metal–Organic Frameworks. *Chem. Sci.*, 9, 3508–3516.

Liu, C. S.; Zhang, Z. H.; Chen, M.; Zhao, H.; Duan, F. H.; Chen, D. M.; Wang, M. H.; Zhang, S.; Du, M.(2017). Pore Modulation of Zirconium–Organic Frameworks for High-Efficiency Detection of Trace Proteins. *Chem. Commun.*, 53, 3941–3944.

Liu, J.; Canfield, N.; Liu, W. (2016). Preparation and Characterization of a Hydrophobic Metal−Organic Framework Membrane Supported on a Thin Porous Metal Sheet. *Ind. Eng. Chem. Res.*, 55, 3823−3832.

Liu, X; Demir, N. K. Wu, Z; Li, K. (2015). Highly Water-Stable Zirconium Metal-Organic Framework UiO-66. Membranes Supported on Alumina Hollow Fibers for Desalination, *J Am. Chem Soc., 137, 6999-7002.*

Mallik, B. S.; Chandra, A. (2006). Hydrogen Bond and Residence Dynamics of Ion-Water and Water-Water Pairs in Supercritical Aqueous Ionic Solutions: Dependence on Ion Size and Density. *J. Chem. Phys.*, 125, 234502.

Morris, W.;Wang, S.; Cho, D.; Auyeung, E.; Li,P.; Farha, O. K.; Mirkin, C.A.( 2017). Role of Modulators in Controlling the Colloidal Stability and Polydispersity of the UiO-66 Metal−Organic Framework. *ACS Appl. Mater. Interfaces*, 9, 33413−33418.

Nan, J.; Dong, J.; Wang, W.; Jin, W. (2012). Formation Mechanism of Metal–Organic Framework Membranes Derived from Reactive Seeding Approach. *Micro and Meso. Mater.*, 155, 90–98.

Nghiem, L. D.; Schafer, A. I.; Elimelech, M. (2004). Removal of the Natural Hormones by Nanofiltration Membranes: Measurement, Modeling, and Mechanisms. *Environ. Sci. Technol.*, 38, 1888–1896.

Oien, S.; Wragg, D.; Reinsch, H.; Svelle, S.; Bordiga, S.; Lamberti, C.; Lillerud, K. P. (2014). Detailed Structure Analysis of Atomic Positions and Defects in Zirconium Metal-Organic Frameworks. *Cryst. Growth Des.*, 14, 5370−5372.

Peterson, G.W.; Destefano, W.R.; Garibay, S. J.; Ploskonka, A.; McEntee, M.; Hall, M.; Karwacki, J.; Hupp, J. T; Farha, O. K. (2017). Optimizing Toxic Chemical Removal Through Defect-Induced UiO-66-$NH_2$ Metal-Organic Framework *Chem. Eur. J.*, 23, 15918.

Peter-Varbanets, M.; Vital, M.; Hammes, F.; Pronk, W. (2010). Stabilization of Flux During Ultra-Low Pressure Ultrafiltration. *Water Res.*, 44, 3607–3616.

Ragon, F.; Horcajada, P.; Chevreau, H.; Hwang, Y.K.; Lee, U-H.; Miller, S.R.; Devic, T.; Chang, J.S.; Serre, C. (2014). In-Situ Energy-Dispersive X-ray Diffraction for the Synthesis Optimization and Scale-Up of the Porous Zirconium Terephthalate UiO-66. *Inorg. Chem., 53, 2491-2500.*

Schaate, A.; Roy, P.; Godt, A.; Lippke, J.; Waltz, F.; Wiebcke, M.; Behrens, P. (2011). Modulated Synthesis of Zr-Based Metal–Organic Frameworks: From Nano to Single Crystals *Chem. Eur. J*, 17, 6643 – 6651.

Sharma, R. R.; Chellam, S. (2005). Environ. Temperature Effects on the Morphology of Porous Thin Film Composite Nanofiltration Membranes. *Sci. Technol.*, 39, 5022–5030.

Shearer, G. C.; Chavan, S.; Bordiga, S.; Svelle, S.; Olsbye, U.; Lillerud, K. P. (2016). Defect Engineering: Tuning the Porosity and Composition of the Metal-Organic Framework UiO-66 via Modulated Synthesis. *Chem. Mater.*, 28, 3749−3761.

Shen, M.; Keten, S.; Lueptow, R. M. (2016). Rejection Mechanisms for Contaminants in Polymeric Reverse Osmosis Membranes *J. Membr. Science*, 509, 36–47.

Su, J.; Guo, H. (2011). Control of Unidirectional Transport of Single-File Water Molecules through Carbon Nanotubes in an Electric Field., 1, 351–359.

Su, J.; Guo, H. (2012). Effect of Nanochannel Dimension on the Transport of Water Molecules. *J. Phys. Chem. B*, 116, 5925−5932.

Taddei, M. (2017). Review When Defects Turn into Virtues: The Curious Case of Zirconium-Based Metal-Organic Frameworks. *Coord. Chem. Rev.*, 343, 1–24.

Tang, X.; Yan, Xiong.( 2017). Dip-Coating for Fbrous Materials: Mechanism, Methods and Applications. *J. Sol-Gel Sc. and Technol.*, 81, 378–404.

Trinh, D.X.; Tran, T.P.N.; Taniike, T.(*2017*). Fabrication of New Composite Membrane Filled with UiO-*66* Nanoparticles and Its Application to Nanofiltration. *Sep. Purif. Technol.,*177, 249 *–256.*

Valenzano, L.; Civalleri, B.; Chavan, S.; Bordiga, S.; Nilsen, M.H.; Jakobsen, S.; Lillerud, K.P.; Lamberti, C. (2011). Disclosing the Complex Structure of UiO-66 Metal Organic Framework: A Synergic Combination of Experiment and Theory. *Chem. Mater., 23, 1700-1718.*

Wan, L.; Zhou, C.; Xu, K.; Feng, B.; Huang, A. (2017). Synthesis of Highly Stable UiO-66-$NH_2$ Membrane with High Ions Rejection for Seawater Desalination. *Micro. and Meso. Mater.*, 252, 207-*213.*

Wang, C.; Liu, X.; Demir, N.K.; Chen, J.P.; Li, K.(*2016*). Applications of Water Stable Metal-Organic Frameworks. *Chem. Soc. Rev*, , 45,5107–*5134.*

Wang, X. L.; Tsuru, T.; Togoh, M.; Nakao, S. I.; Kimura, S. (1995). Evaluation of Pore Structure and Electrical Properties of Nanofiltration Membranes. *J. Chem. Eng. Jpn.*, 28, 186192.

Wu, F.; Lin, L.; Liu, H.; Wang, H.; Qiu, J.; Zhang, X. (2017). Synthesis of Stable UiO-*66* Membranes for Pervaporation Separation of Methanol/Methyl Tert-Butyl Ether Mixtures by Secondary Growth. *J. Membr. Sci.,* 544, 342–*350.*

Wu, H.; Chua, Y. S.; Krungleviciute, V.; Tyagi, M.; Chen, P.; Yildirim, T.; Zhou, W. (2013). Unusual and Highly Tunable Missing-Linker Defects in Zirconium Metal-Organic Framework UiO-66 and Their Important Effects on Gas Adsorption. *J. Am. Chem. Soc.*, 135, 10525−10532.

Zhang, L.; Shi, G. Z.; Qiu, S.; Cheng, L. H, Chen, H. L. (2011). Preparation of High-Flux Thin Film Nanocomposite Reverse Osmosis Membranes by Incorporating Functionalized Multi-Walled Carbon Nanotubes. *Desalination Water Treat.* 34, 19-24.

Zhang, R.; Ji, Wang, S. L.; Wang, N.; Zhang, G.; Li. J. R. (2014). Coordination-driven in Situ Self-Assembly Strategy for the Preparation of Metal-Organic Framework Hybrid Membra. Angew. *Chem. Int. Ed.*, 24, 9775-*9779.*

Zhao W, Zhang C, Yan Z, Zhou Y, Li J, Xie Y, (2017). Preparation, Characterization, and Performance Evaluation of UiO-66 Analogues as Stationary Phase in HPLC for the Separation of Substituted Benzenes and Polycyclic Aromatic Hydrocarbons. *PLoS ONE*,12, e0178513.

Zhu, Y.; Gupta, K. M.; Liu, Q, (2016). Synthesis and Seawater Desalination of Molecular Sieving Zeolitic Imidazolate Framework Membranes. *Desalination*, 385 75-82.

Zornoza, B.; Martinez-Joaristi, A.; Serra-Crespo, P.; Tellez, C.; Coronas, J.; Gascon J.; Kapteijn, F. (2011). Functionalized Flexible MOFs as Fillers in Mixed Matrix Membranes for Highly Selective Separation of $CO_2$ from $CH_4$ at Elevated *Pressures. Chem. Commun*, 47, 9522–9524.